

To be published in Astronomical Journal, Oct 1995

Faintest Galaxy Morphologies from *HST* WFPC2 Imaging of the Hawaii Survey Fields¹

Lennox L. Cowie, Esther M. Hu, and Antoinette Songaila

Institute for Astronomy, University of Hawaii, 2680 Woodlawn Dr., Honolulu, HI 96822
cowie@ifa.hawaii.edu, hu@ifa.hawaii.edu, acowie@ifa.hawaii.edu

ABSTRACT

We present very deep *HST* WFPC2 images in the F814W filter of two Hawaii Survey fields, SSA13 and SSA22. Using these data with previous ground-based imaging and spectroscopy, we compare the colors, star-forming properties and morphologies of the faintest galaxies with a reference sample of bright nearby galaxies and analyze the changes in field galaxy morphology with magnitude. Our principal result is the identification of a new morphological class of “chain” galaxies at the faintest magnitudes. Based on limited spectroscopy, we tentatively conclude that these are linearly organized giant star-forming regions at $z = 0.5-3$ and, if this is correct, that these are large galaxies in the process of formation.

Subject headings: cosmology: early universe — cosmology: observations — galaxies: evolution — galaxies: photometry — infrared: galaxies

1. Introduction

A question fundamental to the understanding of galaxy evolution is how the properties of galaxy types evolve with redshift, and indeed, whether any distinctly new classes of objects appear at high redshifts and faint magnitudes. Extensive recent work on faint galaxy imaging samples (*e.g.*, Tyson 1988; Lilly, Cowie, & Gardner 1991, hereafter LCG; Gardner, Cowie & Wainscoat 1993, Glazebrook *et al.* 1994a; Cowie *et al.* 1994, hereafter Paper I; Cowie

¹Based on observations with the NASA/ESA *Hubble Space Telescope* obtained at the Space Telescope Science Institute, which is operated by AURA, Inc., under NASA contract NAS 5-26555.

et al. 1995, hereafter Paper II; Metcalfe *et al.* 1995; Djorgovski *et al.* 1995; Glazebrook *et al.* 1995a) has explored color and number-count distributions at both bright and faint magnitudes. These surveys find a strong excess of blue objects at faint magnitudes (by factors of ~ 2 or more over predictions with no galaxy luminosity evolution by $B = 24$). Spectroscopic studies (Broadhurst, Ellis, & Shanks 1988; Colless *et al.* 1990; LCG; Cowie, Songaila, & Hu 1991, hereafter CSH; Loveday *et al.* 1992; Tresse *et al.* 1993; Lilly 1993; Songaila *et al.* 1994, hereafter Paper III; Glazebrook *et al.* 1995b) have shown that the bulk of galaxies studied to $K = 19$, $I = 22$, and $B = 24$ have redshifts $z \lesssim 1$ and that a large fraction of the strong excess of very blue objects at faint magnitudes can be identified with relatively low-mass gas-rich systems at $z \sim 0.4$ (CSH).

In the present paper we study *morphological* changes in field galaxies with redshift using very deep (4.3–8 hr) *HST* WFPC2 images in the ‘wide-*I*’ (F814W) filter on two Hawaii Survey Fields, SSA13 and SSA22. The substantial increase in depth over previous field investigations with *HST* (*e.g.*, Griffiths *et al.* 1994; Glazebrook *et al.* 1995c) permits studies of the very faint-end morphologies and colors, and the construction of *I*-band number counts down to $I=26$; while the availability of previous multi-color imaging on these fields (Paper I) and related wide-field surveys (Paper II), in combination with near-complete spectroscopic coverage over selected subregions (Paper III), allows quantification of changes in color and star-forming properties with redshift. We present a reference atlas of bright nearby galaxies, with $K \leq 14$, spectroscopically studied and with similar linear resolution and S/N to the *HST* observations, and compare it with the assembled atlas of objects from the *HST* samples. In addition, as we have stressed in Paper I, the *K*-band data on these samples permits a magnitude-limited sample selection that is not biased by the type mix of galaxies being studied, since magnitudes selected in the *K*-band, as opposed to the *B*- and even the *I*-band, are insensitive to highly variable *K* corrections that, at optical wavelengths, depend on both the morphological type and redshift of the objects measured.

The major result of the present paper is the identification of a new morphological class of objects at the faintest magnitudes. We call these ‘Chain’ galaxies, and they appear as extremely narrow, linear structures (barely resolved by the WFC in the transverse direction) with superposed bright ‘knots’. The chains can be identified with a spectroscopically distinct class of very blue (flat-spectrum) objects, which onsets in substantial numbers (about 2 arcmin⁻² at $B \sim 24$) at approximately $B = 23$ (cf. LCG), and which comprises 20–50% of the population identified with the strong excess in blue number counts.

The acquisition, processing, and calibration of the WFC2 data are described in §2. A summary of the number counts and colors, showing the strong blueing trend at faint magnitudes is given in §3. A qualitative description of the galaxy morphologies considered

in terms of various color selection criteria is presented in §4, along with a description of the characteristics and statistics of the faint blue populations. §5 discusses the properties of the chain galaxies in the context of possible models for their formation and their extreme linear structure. A quantitative analysis of the galaxy morphologies and surface brightness profiles will be given in a second paper (Hu *et al.* 1995).

2. Observations

WFPC2 integrations were taken on two of the Hawaii Galaxy Survey fields (which are defined in LCG and Paper I): the SSA22 field was observed with the F814W filter on the WFPC2 (twelve 2400 s exposures on 1994 November 21 and 26) and the SSA13 field in the same configuration (six 2600 s exposures on 1995 January 30). Each exposure was dithered by a five arcsecond step from the previous one. The pipeline-processed flattened and calibrated images were used. The sky was determined from the median of the individual frames and a normalized version subtracted from each frame. The frames were then resampled to 1600×1600 pixels and registered. Cosmic rays were removed by comparing each pixel with the median of the pixels in all the frames and rejecting those which deviated by more than 3σ . The frames were finally summed. The images of the three WFC2 frames on each field are shown as Figures 1 and 2 (Plates 1 and 2). The final full width half maximum (FWHM) was measured as $0''.22$ on the SSA22 images and $0''.19$ on the SSA13 image.

The photometric system was derived from the PHOTFLAM calibration generated in the pipeline process with 0 mag corresponding to the Kron-Cousins *I*-band zeropoint of 1.22×10^{-9} ergs cm^{-2} s^{-1} \AA^{-1} from Bessell (1979). For the WFC chip 2 this corresponds to

$$I_{HST} = 30.12 - 2.5 \log_{10}(\text{DN}) \quad (1)$$

where DN is the number of counts in a 2400 s interval in the F814W filter. For the faint galaxy photometry of the present paper we have adopted corrected aperture magnitudes using a $1''.6$ diameter aperture offset by -0.16 mag to correct to total magnitudes. The offset was measured by comparison with $6''$ diameter aperture magnitudes. The $1''.6$ diameter aperture is the smallest usable aperture in which the correction to total magnitude is relatively invariant from object to object. This is illustrated in Fig. 3, where we show the difference between $1''.6$ and $3''.2$ diameter aperture magnitudes for isolated objects in the fields; the spread in total magnitudes corresponds to an uncertainty of approximately ± 0.2 mag in the total magnitude of an object, which we consider acceptable for the present type of work. For smaller apertures the spread rises rapidly.

The I_{HST} magnitudes closely approximate the ground-based I magnitudes of Paper I. In Fig. 4 we show $(I_{HST} - I)$ vs $(B - I)$ where I and B are from papers I and II. The least squares fit gives a small color term $-0.08 + 0.05(B - I)$ and a dispersion of 0.14 mag. For the present purposes we ignore the color term and use I_{HST} and I interchangeably. Because of the characteristic flat spectrum of many sources, it has sometimes been the convention to quote object magnitudes in terms of AB magnitudes – a system where the zero-points for the various color bands B_{AB} , I_{AB} , and K_{AB} coincide for objects which are flat in f_ν . Following the discussion of LCG, we give the conversion between Kron-Cousins I magnitude and I_{AB} as $I \sim I_{AB} - 0.48$, and $B \sim B_{AB} + 0.17$ and $K \sim K_{AB} - 2.0$ for Johnson B and K . We shall occasionally move to the AB system where it is appropriate.

For each field a primary catalog was generated of all objects with surface brightness above $24.7 \text{ mag arcsec}^{-2}$ in a $0''.2$ boxcar-smoothed image. Objects with centers closer than $1''.6$ were then combined and the magnitudes measured following the procedure outlined above. The star-galaxy separation was made using the inverse second moment classifier (Kron 1980). B and K magnitudes for the I -selected samples were obtained for the object list from the ground-based data using the procedures outlined in Paper I. In addition, I magnitudes were measured from the HST data for ground-based K - and B -selected samples.

The noise levels for each field were next determined by measuring the dispersion of the signal from blank sky positions on each image. The 1σ level for the corrected total magnitudes is similar for the 13- and 22-hr fields at $I = 27$, since the 13-hr field is at much higher ecliptic latitude and the background is $22 \text{ mag arcsec}^{-2}$ vs $21.5 \text{ mag arcsec}^{-2}$ for the 22-hr field.

Finally, the incompleteness of the object recovery was measured as a function of magnitude. We adopted the procedure of adding, to the data in each WFC2 chip, field data from another of the two WFC2 fields reduced by a factor of 10, and then re-running the cataloging procedure. The fraction of the added objects which were retrieved was then determined. The incompleteness becomes substantial at magnitudes greater than $I = 25$: only 52% of objects between $I = 25$ and 26 were recovered. We have therefore computed the galaxy counts only to $I = 26$.

3. Counts and Colors

The I band counts from the two fields are shown in Fig. 5. They extend the previous deepest I -band counts from ground based data by about 1.5 mag to $I = 26$ ($I_{AB} = 26.5$),

and there is good agreement with the ground-based data in the region of overlap (Tyson 1988; LCG). The faint I counts are well fit by the power law $dN/dm = 240 \times 10^{0.37(I-17)}$ galaxies $\text{deg}^{-2} \text{mag}^{-1}$.

The galaxy counts are now becoming very well defined to extremely faint magnitudes over the full optical and near-IR range. Fig. 6 shows a compilation of recent faint K -band counts from a number of groups. These are well fit by $dN/dm = 1460 \times 10^{0.25(K-15)}$ from $K = 17$ to $K = 24$, or equivalently, $K_{AB} = 26$. The faint B -band counts have recently been summarized by Metcalfe *et al.* (1995) and to $B = 27$ ($B_{AB} = 26.8$) have the form $1.0 \times 10^{0.42(B-14)}$. The counts in each color are compared in Fig. 7, which shows just how remarkable the blueing trend in the galaxy population really is. At the faintest AB magnitudes ($AB = 26$) the K counts have fallen below the I counts, and both have closely approached the B counts. This requires that the vast majority of the faintest galaxies are very blue, with spectra close to flat f_ν over the full range $4000 \rightarrow 25,000 \text{ \AA}$.

At slightly brighter magnitudes we can investigate the colors of individually selected galaxies. Fig. 8 shows the $(I - K)$ colors of a $K = 22$ sample selected from the ground-based data. The substantial improvement in the S/N of the I -band data obtained with *HST* now allows us to see that at the faint end the population is dominated by blue $(I - K)$ galaxies, with a small number of very red $(I - K)$ objects. At $K = 21 \rightarrow 22$ the median color is therefore very blue with $\langle(I - K)\rangle = 2.1$ (only 0.6 mag redder than flat f_ν), but this is determined by 80% of the objects (12 out of 15). The remaining 20% (3 out of 15) are quite red.

Fig. 9 shows the $(B - I)$ colors of an $I \leq 25$ sample selected from the full *HST* data. At $I = 25$ the median $(B - I)$ color of a galaxy is only 1.2, less than 0.5 mag different from flat-spectrum.

4. Galaxy Morphology

4.1. K -Selected Samples

For the purposes of studying the morphology of normal galaxies at $z \sim 1$ it is almost essential to use a near-infrared selection, since even an I -band selection results in K correction biases against higher redshift elliptical and spiral galaxies (Paper I). As a result, direct selection from the *HST* data results in a serious bias to lower z and blue galaxies. For our

primary analysis, therefore, we have used the K -band selected samples of Papers I and III to define the sample, and then used the HST I -band images to study the morphology.

At $K \leq 18.5$ (Fig. 10, Plate 3) we show all the objects in the HST fields. The K -band magnitudes (lower left corner of each panel) are taken from the K -band strip data of Paper III. In order to provide uniform contrast we have normalized each image by its I -band flux so that sky noise levels appear higher for the fainter objects. All of the objects have spectroscopic identifications either from Paper III or from subsequent observations with the LRIS spectrograph on the Keck 10 m telescope (Songaila *et al.* 1995). The galaxy redshifts are presented in the lower right corner of each panel. Fig. 11 (Plate 4) shows the corresponding data for $K = 18.5 - 19.5$ selected from the strips for the 22-hr field where the strip image is much deeper, but only in the deep field region of Paper I in the 13-hr field. Finally, Fig. 12 (Plate 5) shows the data for a $K = 19.5 - 20$ sample selected from only the deep field K samples of Paper I. All but three galaxies of the $K < 19.5$ sample have measured redshifts, but only slightly less than half of the $19.5 - 20$ sample do.

We can see from the plates that at $K \leq 19.5$ we appear to be selecting a rather normal population of galaxies. The redshift data show that nearly all of these objects are at $z \lesssim 1$. For comparison we have shown a ground-based complete $K \leq 14$ selected sample (Fig. 13, Plate 6) of 25 spectroscopically identified galaxies displayed at a similar linear scale and S/N as the HST data. As we shall address more quantitatively in the second paper (Hu *et al.* 1995), the distribution of types and sizes is remarkably similar between the bright and faint samples.

At $K \geq 19.5$ the morphologies of the galaxies become much more diverse. Fig. 12 continues to show some galaxies with relatively normal appearance, but there is now a large fraction of amorphous and distorted galaxies, as well as a population (#s 6, 16, and 19) of just-resolved, symmetric objects which are very faint in the I band.

The onset of the morphology change corresponds to the onset of the blueing of the K -selected samples, and the bifurcation into blue and red populations in the color-magnitude diagram of Fig. 8; it may also be associated with the movement of the maximum redshift beyond $z = 1$. At $z > 1$, as the 4000 \AA break moves through the I band, galaxies fade rapidly and the redder objects in the $19.5 - 20$ sample most probably correspond to the high-redshift ($z > 1$) tail of spirals or ellipticals (Paper I).

The simultaneous appearance of the amorphous galaxies is more surprising. For the small number of galaxies where redshifts have been measured these are emission-line objects at moderate redshift ($z \sim 0.4$). At $K = 19.5 - 20$ they constitute almost half the objects and completely dominate the blue populations. The most likely explanation is that because of

volume geometry effects and/or galaxy evolution we are seeing relatively few high- z galaxies, and that as we move to fainter magnitudes our samples are rapidly becoming dominated by the faint end of the luminosity function of modest redshift galaxies. The faint end slope of the counts and the blueing trend then correspond to the shape and colors of the faint end of the luminosity function.

At fainter magnitudes we have constructed a $K = 20.5 - 22$ atlas for the 22-hr deep field and a $K = 20.5 - 21.5$ atlas for the 13-hr deep field (Figs. 14 and 15, Plates 7 and 8). There is very little redshift information for this faint end sample; however, at these K magnitudes the population is dominated by the blue ($I - K$) galaxies: only 9 objects have ($I - K$) colors even in excess of 3. Unusual morphologies also dominate at the faint end: roughly half of these unusual objects are the amorphous galaxies that are the majority of the $K = 20$ counts, but now we also see a considerable population of a new class of object which appears narrow and linear, and often has a beaded morphology. Prototype examples are objects 4, 5, 9, and 15 of Fig. 14. A substantial fraction of the $K = 20.5 - 22$ galaxies fall into this category. They appear similar to the morphological class of chain galaxies in the Arp atlas (1966) and we shall refer to them as chain galaxies in the subsequent text.

To loosely quantify these changes in the mix of morphologies we have adopted a crude galaxy classification in which galaxies with a strong nucleus and surrounding smooth envelope are classified as Type 1, those with a strong nucleus and apparent spiral arm structure as Type 2, and those with an amorphous appearance as Type 3. Very roughly, Type 1 includes the Hubble types E/S0/Sa, Type 2 the Sb's and Sc's, and Type 3 the Sd's and Im's. We have also distinguished two further classes of galaxies – Type 4, corresponding to galaxies with strong signs of interaction, and Type 5, corresponding to the chain galaxies described above. Glazebrook *et al.* (1995c) have used a similar breakdown in analyzing the Medium Deep Survey but with our types 3–5 combined into a single category of peculiar and merging galaxies. The distinction between Type 1 and Type 2 is poorest, and becomes very uncertain at the faintest magnitudes, but the remaining types are easily picked out.

We have summarized the distribution of types vs K magnitude in Fig. 16. At $K < 19$ nearly all galaxies are Type 1 or Type 2 in roughly equal numbers with a small admixture of interacting galaxies (Type 4). At $K > 19$ the Type 3 galaxies appear in substantial numbers, while at $K > 20.5$ the chain galaxies of Type 5 become the largest class.

As Glazebrook *et al.* (1995c) have emphasized, this rapid evolution in morphology has major implications for interpreting galaxy number counts. In Fig. 17 we show the fraction of galaxies in the K -band counts that fall into the Type 1 and 2 categories. This ‘normal’ fraction has dropped to less than 20% at $K = 21$. Glazebrook *et al.* have argued that the B -band galaxy counts may be modelled by including the normal population (here Types 1

and 2) with no evolution in the number density or luminosity, and then adding the rapidly evolving population of peculiar and interacting galaxies (here Types 3–5). However, this model does not provide an adequate description of the K counts. As Gardner *et al.* (1993) have shown, there is an excess of K counts at $K = 17$ over models in which there is no luminosity evolution. However, from Figs. 16 and 17 we can see that at this magnitude there is very little contamination by the Type 3–5 populations which therefore cannot be the explanation for this excess.

It is probable that the Type 1 and 2 galaxies are also evolving, and this evolution may well be correlated with the onset of the other types. If this is true we will need to develop a wider understanding of the nature of the evolution before we can begin fully to reinterpret the number counts.

4.2. Blue-Selected Samples

Because the anomalous faint-end population is so blue we have also considered the morphology in the B -selected sample. For each of the two fields a complete $B = 24.5$ atlas was formed in the three *HST* WFC areas. The 71 objects in the sample are shown in Figs. 18 and 19 (Plates 9 and 10). Each frame in these plates is $3''2$ on a side. The B magnitude is shown in the lower left corner and the redshift (where known) in the lower right corner. At least 6 of the magnitude-selected sample are stars based on the spectroscopic observations while 21 of the objects are very blue, satisfying the color criterion $(B - I) < 1.4$ (Paper I). These latter objects are marked ‘flat’ in the upper right hand corner. All but one of the spectroscopically observed objects at $B \leq 24$ have been identified. At $B \leq 23$ all objects are at $z \leq 1$ whereas for $23 \leq B \leq 24$, 6 of the 23 objects with redshifts are at $z > 1$. This redshift distribution in the *HST* fields is consistent with the much larger sample of Songaila *et al.* (1995).

Inspection of Plates 9 and 10 shows that the flat spectrum galaxies are split into several morphological classes. There are low-redshift extragalactic H II regions and Im galaxies such as object 8 in Fig. 19 and object 4 in Fig. 18, which are at very modest redshifts. These are small diffuse objects, and roughly a third of the $B \leq 24.5$ flat-spectrum objects fall into this morphology class. However, many of the remaining flat objects consist of the chain galaxies noted in the K -band data. A further unusual multicellular morphology which may be related in some way to the chains is seen in object 26 of Fig. 18, where a set of blobs is immersed in a more diffuse circular envelope. The object with peculiar morphology reported by Glazebrook *et al.* (1994b) may be a bright example of this class. The remaining flat spectrum galaxies

have single or slightly elongated very marginally resolved images. Examples are objects 8 and 9 in Fig. 18. If the chain galaxies are linear, some of these objects could correspond to chain galaxies seen in projection.

Clearly defined chain galaxies comprise 6 of the 41 galaxies in the $23.5 \rightarrow 24.5$ magnitude range (objects 11, 23 and 29 in Fig. 19 and objects 15, 17, and 25 in Fig. 18) while more questionable cases could roughly double this number. Thus the chains constitute 15 – 30% of the objects at $B = 24$ and do not comprise the majority of the excess blue counts seen at this magnitude, which appears to be produced by a combination of the chains and of the excess number of low redshift galaxies. The exact value of the blue excess at $B = 24$ is uncertain, but lies between a factor 2 and 4 (*e.g.*, Tyson 1988; LCG; Metcalfe *et al.* 1991; Glazebrook *et al.* 1995a). This means that in rough terms the chain galaxies may contribute 20 – 50% of the excess at this blue magnitude.

5. The Chain Galaxies

The chain galaxies seem to be a new class of object which appears in the faintest magnitude samples and is associated in part with the extreme blueing seen in the faint galaxies. Their curious morphologies and high spatial frequency make them an extremely interesting class.

To determine the spread in the properties of the chain galaxies, we have formed an atlas of all galaxies with $I < 25$ in the *HST* fields that clearly show the chain morphology. The 26 objects selected in this way from the two fields are shown in Figures 20a–c (Plates 11, 12 and 13) and their properties are summarized in Table 1 where we give the K , I and B magnitudes, the transverse width when the point spread function is deconvolved, and an axial ratio, defined here as the ratio of the longitudinal to transverse lengths of the undeconvolved surface brightness contour corresponding to 20% of the peak surface brightness.

The chain galaxies are uniformly blue at the brighter magnitudes where the colors can be measured reliably. In Fig. 21 we compare the $(B - I)$ colors of chains with $I < 24$ with the full sample of $I < 24$ galaxies. The chains clearly fall along the lower envelope of the field galaxies, having a median $(B - I) = 1.6$. The uniformly blue color of the sample argues that, irrespective of the origin of the light, the objects cannot be at redshift $z \gg 3$ since otherwise some would lie behind intergalactic clouds which are opaque beyond the wavelength of the Lyman limit and would extinguish the B light. (cf. Madau [1995] for a recent discussion of this effect.) The chains are also extremely blue in $(B - K)$ (Table 1) and are generally only

marginally detected in K . This rules out the possibility that we are seeing relatively normal galaxies in the rest ultraviolet and that the peculiar morphologies are a consequence only of the distribution of the star-forming regions.

Morphologically, we find that the chains are extremely narrow in their transverse extent, being only marginally resolved in the transverse dimension with sizes $\sim 0''.05 - 0''.1$. The longitudinal sizes are around $2 - 3''$. (The measured dimensions are summarized in Table 1.) These very large ellipticities argue strongly against these being any class of edge-on object. The linear extent of each blob in the chain is similar to their transverse dimensions while blob separations are about $0''.5$, or several times larger (cf. Fig. 22).

The extremely narrow transverse widths argue against the chain population being local, since at redshifts where the Euclidean approximation is valid the transverse dimensions are only

$$r = 10 \text{ pc} \left(\frac{z}{0.01} \right) \left(\frac{\sigma}{0''.05} \right) h_{75}^{-1} \quad (2)$$

where h_{75} is the Hubble constant in units of $75 \text{ km s}^{-1} \text{ Mpc}^{-1}$ and σ is the transverse dimension in arcseconds. If we assume instead that the chains are at redshifts $z \gtrsim 0.5$ then the individual blob dimensions correspond to a linear size of $\sim 0.5 - 1 h_{75}^{-1} \text{ kpc}$. The spread in the transverse sizes is also quite small, only a factor of four. This also suggests that the objects must lie at $z \gtrsim 0.5$ where the angular distance becomes relatively invariant since otherwise they would have to be confined to a narrow shell in redshift.

We have some limited spectroscopic information on the brighter chain galaxies. Chains 0 and 1 of Fig. 20a are emission line galaxies at $z = 0.489$ and $z = 0.505$, respectively. Two further objects, SSA22–16 and SSA22–24, were identified as unusually blue in the LCG sample and were the subject of intensive study. SSA22–16 (which is object 4 in Fig. 14 and object 3 in Fig. 20a) has a strong emission line and appears to lie at $z = 1.36$ (Fig. 23). In contrast, the optical spectrum of SSA22–24 (object 9 in Fig. 14 and object 6 in Fig. 20a) is featureless except for a continuum break near 4000 \AA in the observed frame (LCG). The simplest explanation of the color and spectral information is that the chain galaxies are intense star forming galaxies which, if the [O II] line has redshifted out of the optical window at $z > 1.6$, appear as relatively featureless flat spectrum objects until the $\text{Ly}\alpha$ wavelength moves into the observable window at $z \sim 2$. $\text{Ly}\alpha$ emission is weak, analogous to low-redshift extragalactic H II regions and Im's, but the imposed signature of the intergalactic $\text{Ly}\alpha$ forest produces a partial break at shorter wavelengths (Madau 1995). This interpretation of the break in SSA22–24 would then place it at $z = 2.4$.

While recognizing the indirect nature of these arguments and the limited nature of the spectroscopic information, we therefore suggest that the chain galaxies consist of star-

forming regions and lie in the redshift range, $z \sim 0.5 - 3$. At these redshifts the typical chain would contain about 10^9 OB stars and have a mass larger than or comparable to that of a present-day galaxy.

This brings us finally to the strangest feature of the galaxies — their linear structure. Given the ubiquity of these objects, we assume that this is not a gravitational lensing phenomenon but rather represents their intrinsic nature. Since the linear morphologies are inherently unstable and will disrupt on a timescale comparable to the transverse crossing time which is only

$$t = 3 \times 10^7 \text{ yr} \left(\frac{r}{1 \text{ kpc}} \right) \left(\frac{10 \text{ km s}^{-1}}{v} \right) \quad (3)$$

where v is the transverse velocity, it is probable that we are seeing the structures in the process of formation. The simplest explanation may be that linear structures form during the collapse of the protogalactic gas and when star formation turns on it triggers induced star formation along the line of maximum density — a process analogous to the sequential propagation of OB star associations in molecular clouds in our own galaxy. However, there may be other mechanisms — such as string-induced wakes (Brandenberger 1991) — which might more naturally produce a linear structure.

6. Conclusion

Using *HST* *I*-band images of a K -selected galaxy sample, we have shown that the faint-end galaxy counts at $K \geq 19$ are dominated by blue galaxies with unusual morphologies and that at $K > 20$, the largest single class is a new type of galaxy with linear, often beaded, structure which we refer to as a chain galaxy.

Based on indirect evidence and our limited spectroscopic information, we have argued that the chain galaxies are lines of giant star-forming regions at redshifts between 0.5 and 3. If this interpretation is correct, then the chains are very large galaxies in the process of formation.

The key question remaining is whether the chains are a transient population of galaxies unrelated to present-day galaxies or whether they are their lineal ancestors. Songaila, Cowie & Lilly (1990) have given model-independent arguments that the blue galaxy population, of which the may chains comprise a major part, do contain enough star formation to be the progenitors of present-day galaxies. However, in this case we would expect to see ‘missing links’ with morphologies intermediate between the chains and current galaxies. One candidate is the amorphous multicellular galaxies described here and in Glazebrook *et al.* (1994b)

which could represent the first stage in the dissolution of the linear structure of the chains prior to the onset of more normal spiral morphology. Investigation of the kinematics and colors of these objects should determine if this is a tenable hypothesis.

REFERENCES

- Arp, Halton 1966, ApJS, 14, no. 123 [Atlas of Peculiar Galaxies]
- Bessell, M. S. 1979, PASP, 91, 589
- Brandenberger, R. H. 1991, Phys. Scripta, T36, 114
- Broadhurst, T. J., Ellis, R. S., & Shanks, T. 1988, MNRAS, 235, 827
- Colless, M. M., Ellis, R. S., Taylor, K., & Hook, R. N 1990, MNRAS, 244, 408
- Cowie, L. L., Gardner, J. P., Hu, E. M., Songaila, A., Hodapp, K.-W., & Wainscoat, R. J. 1994, ApJ, 434, 114 (Paper I)
- Cowie, L. L., Songaila, A., & Hu, E. M. 1991, Nature, 354, 460 (CSH)
- Cowie, L. L., Wainscoat, R. J., & Gardner, J. P. 1995, in preparation (Paper II)
- Djorgovski, S., Soifer, B. T., Pahre, M. A., Larkin, J. E., Smith, J. D., Neugebauer, G., Smail, I., Matthews, K., Hogg, D. W., Blandford, R. D., Cohen, J., Harrison, W., & Nelson, J. 1995, ApJ, 438 L13
- Gardner, J. P., Cowie, L. L., & Wainscoat, R. J. 1993, ApJ, 415, L9
- Glazebrook, K., Peacock, J. A., Collins, C. A., & Miller, L. 1994a, MNRAS, 266, 65
- Glazebrook, K., Léhar, J., Ellis, R., Aragon-Salamanca, A., & Griffiths, R. 1994b, MNRAS, 270, P63
- Glazebrook, K., Ellis, R., Colless, M., Broadhurst, T., Allington-Smith, J., & Tanvir, N. 1995a, MNRAS, 273, 157
- Glazebrook, K., Peacock, J. A., Miller, L., & Collins, C. A. 1995b, MNRAS, in press
- Glazebrook, K., Ellis, R., Santiago, B., & Griffiths, R. 1995c, preprint
- Griffiths, R. E. *et al.* 1994, ApJ, 435, L19
- Hu, E. M., Cowie, L. L., & Songaila, A. 1995, in preparation
- Kron, R. G. 1980, ApJS, 43, 305
- Lilly, S. J. 1993, ApJ, 411, 501
- Lilly, S. J., Cowie, L. L., & Gardner, J. P. 1991, ApJ, 369, 79 (LCG)
- Loveday, J., Peterson, B. A., Efstathiou, G., & Maddox, S. J. 1992, ApJ, 390, 338
- Madau, P. 1995, ApJ, 441, 18
- McLeod, B. A., Bernstein, G. M., Rieke, M. J., Tollestrup, E. V., & Fazio, G. G. 1995, ApJS, 96, 117

- Metcalfe, N., Shanks, T., Fong, R., & Jones, L. R. 1991, *MNRAS*, 249, 498
- Metcalfe, N., Shanks, T., Fong, R., & Roche, N. 1995, *MNRAS*, 273, 257
- Soifer, B. T., Matthews, K., Djorgovski, S., Larkin, J., Graham, J. R., Harrison, W., Jernigan, G., Lin, S., Nelson, J., Neugebauer, G., Smith, G., & Ziomkowski, C. 1994, *ApJ*, 420, L1
- Songaila, A., Cowie, L. L., & Hu, E. M. 1995, in preparation
- Songaila, A., Cowie, L. L., Hu, E. M., & Gardner, J. P. 1994, *ApJS*, 94, 461 (Paper III)
- Songaila, A., Cowie, L. L., & Lilly, S. J. 1990, *ApJ*, 348, 371
- Tresse, L., Hammer, F., Fèvre, O. L., & Proust, D. 1993 *A&A*, 277, 53
- Tyson, J. A. 1988, *AJ*, 96, 1

Fig. 1.— (Plate 1) Cosmic-ray cleaned WFC2 images of the 13-hr field (SSA13) taken in the F814W filter, and assembled as a composite of six 2600 s exposures offset by 5 arcsec in successive exposures obtained over contiguous orbits. Images from each of the three WFC chips (designated chips 2 through 4) are shown, with chip 2 showing a stellar diffraction spike extending diagonally across the frame. The coordinate center for these observations is: $13^{\text{hr}} 10^{\text{m}} 01^{\text{s}}$, $43^{\circ} 00' 32''$ (1950), and each chip is 80 arcsec on a side. The final FWHM of the image is $0''.19$ (no image restoration applied). Each frame has N at the upper right corner and E at the upper left.

Fig. 2.— (Plate 2) WFC2 images of the 22-hr field (SSA22) in the F814W filter. As for Fig. 1, these images were assembled as composites of six successive exposures of 2400 s each, obtained over contiguous orbits on 21 November 1994, and similar set of six exposures obtained on 26 November 1994, for a total exposure of 8 hrs. The final FWHM of the image is $0''.22$. The field is centered on $22^{\text{hr}} 15^{\text{m}} 01^{\text{s}}$, $00^{\circ} 00' 00''$ (1950).

Fig. 3.— A plot of the difference in I_{HST} aperture magnitudes for isolated objects computed with $1''.6$ and $3''.2$ diameters. The spread in total magnitudes corresponds to an uncertainty of approximately ± 0.2 mag. Filled squares represent data from the SSA22 field; pluses are from SSA13.

Fig. 4.— Color conversion between I_{HST} and the Kron-Cousins I magnitudes of Paper I. ($I_{HST} - I$) is plotted vs $(B - I)$ color using the measured I and B magnitudes from Papers I and II. The least squares fit gives a small color term: $-0.08 + 0.05(B - I)$ and a dispersion of 0.14 mag. Squares are SSA22, pluses are SSA13.

Fig. 5.— I -band number counts from the combined SSA13 and SSA22 HST fields. The adopted magnitude limit of $I = 26$ for the galaxy counts was determined from tests on the incompleteness of object recovery at the faint end. The dashed histogram shows the raw HST data points and the solid histogram the counts corrected for incompleteness, with 1σ error bars indicated for each half magnitude bin. Filled squares show the points from the previous ground-based work on the Hawaii Galaxy Survey fields (LCG), which extend to $I = 24.5$. The thick solid lines show the I counts from Tyson (1988). The best power law fits to ground-based and HST I counts are shown as the dotted line.

Fig. 6.— The K -band number counts of several groups are summarized here. The histogram is the summary of Gardner *et al.* (1993) with dashed lines indicating 1σ error bars. The closed box symbols are from Soifer *et al.* 1994, the open boxes are points from McLeod *et al.* 1995, the filled diamonds are from Djorgovski *et al.* 1995, and the stars are from the present work. 1σ error bars are shown with each point. The agreement among the many works is remarkably good. The solid line shows the power law fit given in the text.

Fig. 7.— The number counts in the B (dotted), I (solid), and K (dashed) color bands are compared. AB magnitudes have been used to reference all these curves to a consistent zero-point. The convergence of the K -band number counts with the curves for the I - and B - bands at the faint end is an indication of the strong blueing trend at faint magnitudes.

Fig. 8.— The $(I - K)$ color distribution of a sample selected according to ground-based K magnitude. At the brighter magnitudes ($K < 20$) the open symbols show data from other fields in the Hawaii surveys. At the fainter magnitudes only the data from SSA13 (filled triangles) and SSA22 (filled boxes) are shown using the HST I -band color. The colors spread into very red and very blue objects at faint K magnitudes. 1σ error bars are displayed. The dashed line shows the condition $(I - K) = 1.5$ for flat f_ν galaxies.

Fig. 9.— The $(B - I)$ vs I color distribution for objects with $I \leq 25$, where I magnitudes have been determined from the full set of HST WFC data. Data from SSA13 are shown as filled triangles, and from SSA22 as filled boxes. The dashed line shows the condition $(B - I) = 1.8$ for flat f_ν galaxies. The solid line is the 1σ upper limit on $(B - I)$.

Fig. 10.— (Plate 3) An atlas of all objects in the HST WFC fields with $K \leq 18.5$ from the K -band strip measurements of Paper III. Each object's K magnitude is shown at the lower left of the panel, and the redshift (or designation, 'star') is given at the lower right based on spectroscopic identifications in Paper III, or subsequently taken with the LRIS spectrograph on Keck (Songaila *et al.* 1995). The gray scale has been set for each panel by normalizing the image to the object's I -band flux, in order to provide uniform contrast. Consequently, sky noise levels appear enhanced for the fainter objects. Each panel is $3''.2$ arcsec on a side.

Fig. 11.— (Plate 4) An atlas of $18.5 \leq K < 19.5$ objects in the HST WFC fields. Labeling, scaling, and field of view is given as for Fig. 10 (Plate 3); K -band measurements come from the K strips for the 22-hr field (Paper III), and the deep-field regions of the 13-hr field (Paper I).

Fig. 12.— (Plate 5) An atlas of $19.5 \leq K < 20$ objects in the *HST* WFC fields. Labeling, scaling, and field of view is given as for Fig. 10 (Plate 3); K -band measurements come from the deep-field regions of the 22-hr and 13-hr fields of Paper I.

Fig. 13.— (Plate 6) An I -band atlas of a complete sample of $K \leq 14$ objects from ground-based data. The 25 spectroscopically identified galaxies displayed here are shown as they would appear at $z = 0.3$ with a box size equal to that in Figs. 10–12. The S/N is comparable to that of the objects in Fig. 10, Plate 3.

Fig. 14.— (Plate 7) A $K = 20.5 \rightarrow 22.0$ atlas of *HST* images for objects in the SSA22 deep field. Field sizes and contrast levels are set following the methodology used in Fig. 10. Redshift information is sparse for this faint-end sample, and the panels are labelled according to K magnitude and $(B - I)$ color.

Fig. 15.— (Plate 8) A $K = 20.5 \rightarrow 21.5$ atlas of *HST* images for objects in the SSA13 deep field. As for Fig. 14.

Fig. 16.— Distribution of galaxy types with K magnitude according to the rough classification scheme given in this paper: Type 1 having strong nucleus and surrounding smooth envelope, Type 2 with strong nucleus and apparent spiral structure, Type 3 amorphous, Type 4 merging or interacting, and Type 5 chain galaxies. Filled diamonds represent the magnitude range $K \leq 14$, filled squares $16 \geq K \geq 20$, and pluses $K > 20$. The increase in amorphous (Type 3) and interacting (Type 4) objects can be seen at the fainter K magnitudes, with the majority of $K > 20$ objects falling into either amorphous (Type 3) or chain (Type 5) galaxies.

Fig. 17.— The fraction of Type 1 plus Type 2 galaxies as a function of K magnitude. These classes correspond to the ellipticals, S0s and spirals that constitute the bulk of ‘normal’ galaxies in K -selected samples. As with Fig. 16, there is a noticeable decrease in such objects at faint K magnitudes.

Fig. 18.— (Plate 9) Atlas of $B < 24.5$ selected *HST* objects from the 13-hr deep field. Each frame is $3''2$ on a side, with the B magnitude given in the lower left corner and the redshift (where known) in the lower right corner. The very blue objects $[(B - I), 1.4]$ are labelled ‘flat’ in the upper right corner.

Fig. 19.— (Plate 10) Atlas of $B < 24.5$ selected *HST* objects from the 22-hr deep field. Labeling and field-of-view follows Fig. 16.

Fig. 20.— (Plates 11–13) An atlas of chain galaxies with $I < 25$ in the two fields. Each image is $12''8$ on a side.

Fig. 21.— The distribution of $(B - I)$ colors vs I magnitudes for *HST* WFC2 galaxies (pluses). The chain galaxies are shown with filled squares. Their onset at faint magnitudes and blue colors may be noted.

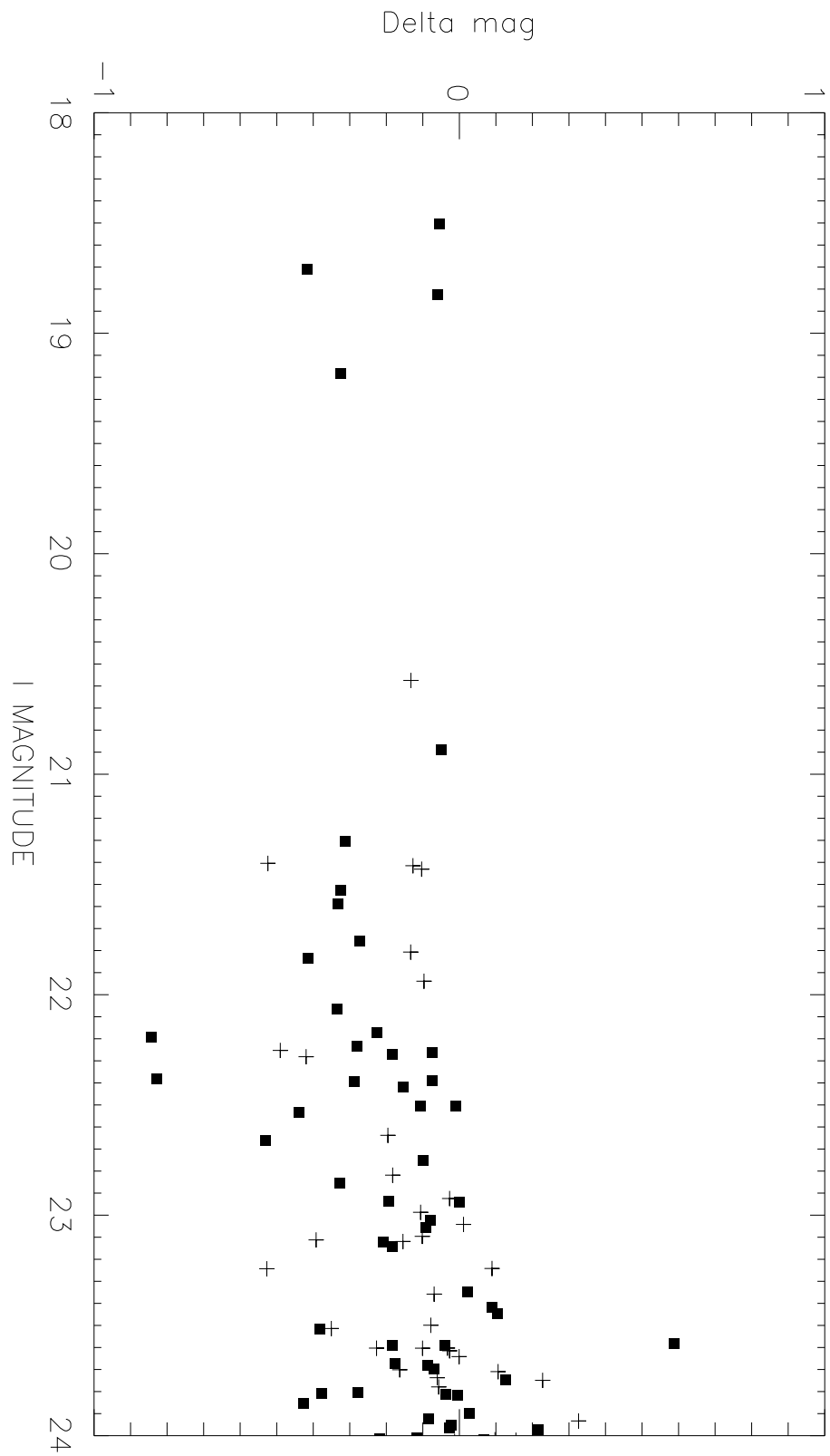
Fig. 22.— The profile along the longitudinal direction for a sample chain galaxy is shown in solid lines, with the very narrow profile along the transverse direction superposed (dashed lines) over one of the bright ‘knots’.

Fig. 23.— Spectrum of SSA 22-16 plotted in the rest-wavelength based on a redshift $z = 1.36$. The hatched regions indicate the positions of strong atmospheric absorption bands. The redshift is based on identifying the strong emission feature as [O II] 3727.

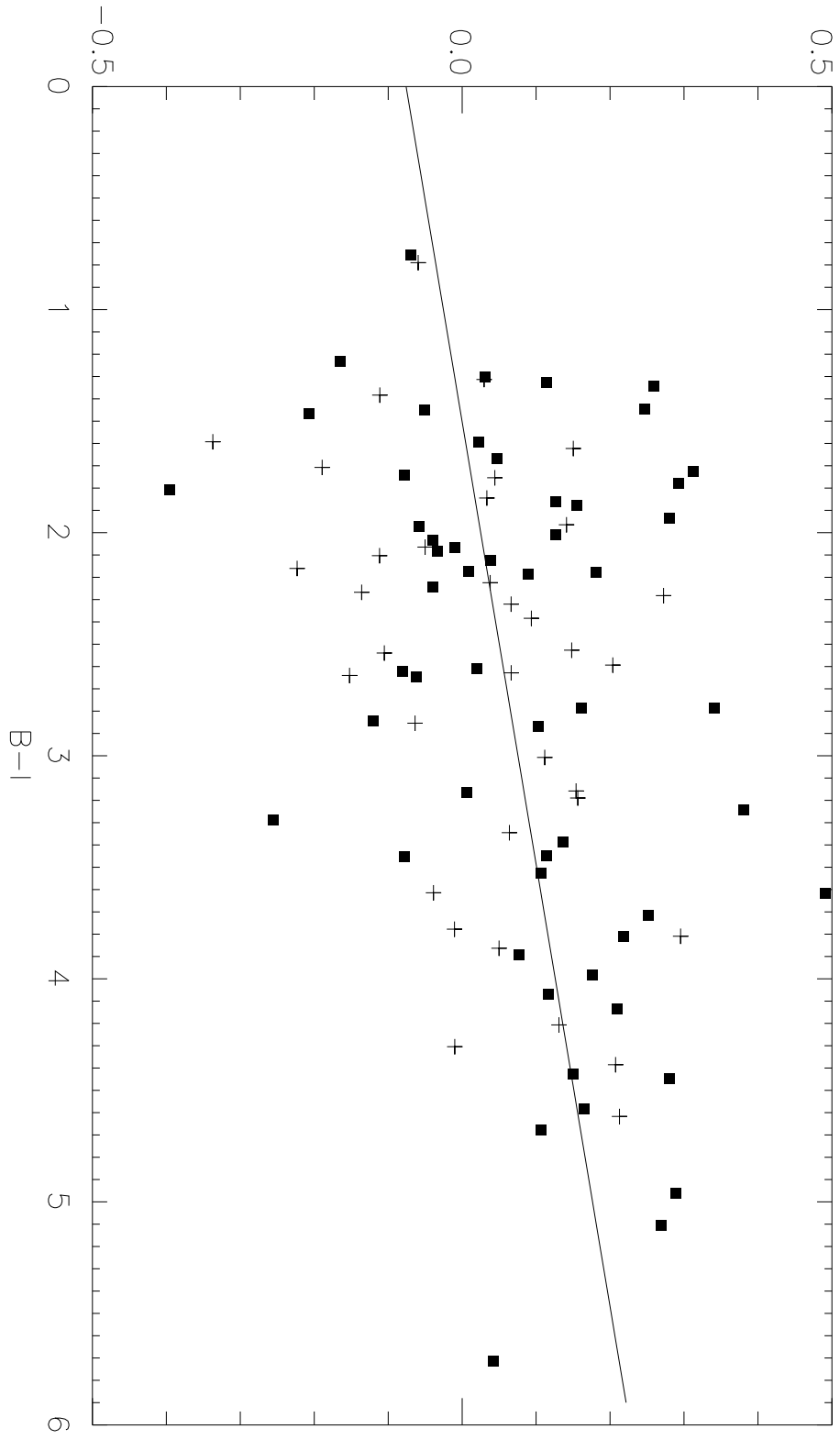
Table 1. Chain Galaxies

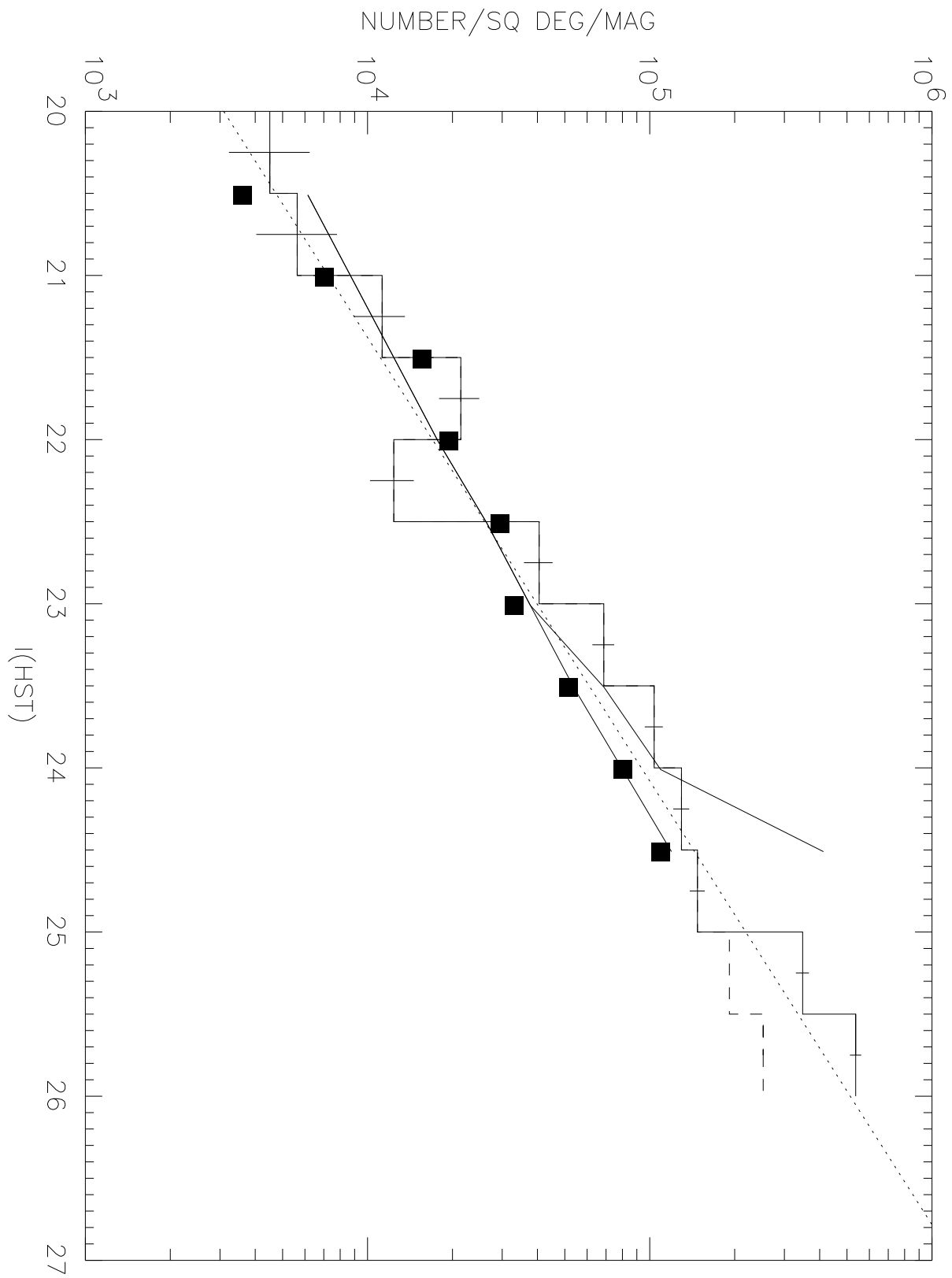
#	I_{HST}	K	B	$(B - I_{HST})$	Transverse σ (arcsec)	Axial Ratio
0	22.2	20.0	24.3	2.1	0.13	4.8
1	22.5	21.1	24.4	1.9	0.14	2.2
2	22.6	0.11	3.4
3	22.7	20.5	23.5	0.8	0.11	5.9
4	22.9	0.23	4.1
5	23.2	-21.9	25.1	1.9	0.09	4.7
6	23.3	20.9	24.1	0.8	0.13	4.3
7	23.3	20.9	25.1	1.8	0.06	9.5
8	23.4	20.5	24.3	0.9	0.05	8.0
9	23.5	22.1	25.1	1.6	0.19	3.2
10	23.6	23.4	24.8	1.2	0.12	3.8
11	23.7	-21.4	25.2	1.5	0.11	3.7
12	23.5	20.5	24.6	1.1	0.17	2.0
13	24.0	-21.3	26.0	2.0	0.12	3.3
14	23.9	21.7	25.5	1.6	0.10	3.9
15	23.8	20.5	24.6	0.8
16	24.0	21.3	25.9	1.9	0.06	8.5
17	24.2	21.3	26.1	1.9	0.07	5.6
18	23.3	-22.4	24.1	0.8	0.18	1.8
19	24.5	21.8	26.3	1.8	0.06	5.3
20	24.4	22.0	25.3	0.9	0.08	...
21	24.6	20.7	24.9	0.3
22	24.7	23.3	25.8	1.1	0.05	6.9
23	24.9
24	25.0	21.6	27.4	2.4	0.10	5.7

Note. — Where the enclosed total flux over the aperture is negative, the magnitude shown reflects the absolute value of the flux, with a leading minus sign.



I(HST)-I(KC)





NUMBER PER SQUARE DEGREE PER MAG

